PLANT IMMUNITY

A helper NLR channels organellar calcium to trigger plant immunity

Tarhan Ibrahim[1]†, Freddie J. King[1]†, AmirAli Toghani[2], Luyao Wang[1], Saskia Jenkins[1], Enoch Lok Him Yuen[1], Hung-Yu Wang[1,3], Cristina Vuolo[1], Nick Eilmann[1], Vanda Adamkova[1], Khong-Sam Chia[4], Baptiste Castel[2], Jonathan D. G. Jones[2], Philip Carella[4], Chih-Hang Wu[3], Jiorgos Kourelis[1]*, Sophien Kamoun[2]*, Tolga O. Bozkurt[1]*

Upon activation, plant nucleotide-binding leucine-rich repeat (NLR) immune receptors are known to assemble into oligomeric resistosomes that insert into the plasma membrane, forming calcium (Ca^{2+})–permeable channels and triggering immunity. Here, we found that the RPW8-like coiled-coil NLR (CC_R-NLR) N requirement gene 1 (NRG1) primarily targets organelles instead of the plasma membrane. Unlike canonical CC-NLRs, activated NRG1 accumulated at the chloroplast envelope and channeled stromal Ca^{2+} into the cytosol. AlphaFold modeling of the NRG1 resistosome revealed an unusually long amino-terminal membrane-insertion structure that could span the double membrane of the chloroplast. Nanobody-mediated relocalization showed functional membrane specificity: Chloroplast trapping abolished activity of the canonical helper CC-NLR NRC4 but not NRG1. NRG1 orthologs, from nonflowering lineages to angiosperms, targeted chloroplasts, suggesting that organelle-centered defense dates back at least ~360 million years. We propose that CC-NLR diversification has enabled compartment-specific immune signaling to capture diverse Ca^{2+} stores.

Innate immunity relies on the precise recognition of pathogens by nucleotide-binding leucine-rich repeat receptors (NLRs), which coordinate defense-related programmed cell death (*1*, *2*). In mammals, activated NLRs assemble into inflammasomes that direct gasdermin oligomers to the plasma membrane, leading to pyroptotic cell death and pathogen clearance (*3*, *4*). Similarly, in plants, activated NLRs assemble into oligomeric structures called resistosomes, some of which target the plasma membrane, ultimately leading to a hypersensitive response (HR) cell death, thereby restricting pathogen invasion (*5*–*8*).

Some NLRs function as singleton receptors to both sense and signal the presence of pathogen effectors. Others operate in specialized pairs or complex networks, where sensor NLRs recognize pathogen effectors and helper NLRs execute the HR. NLRs are multidomain receptors that typically consist of a divergent N-terminal domain, a central NB-ARC domain, and a C-terminal leucine-rich repeat (LRR) domain. Phylogenetic classification divides flowering plant NLRs into four major classes, each characterized by specific N-terminal domain architectures: Toll/interleukin-1 receptor (TIR)–NLRs and three types of sequence-unrelated but structurally and functionally conserved four-helix coiled-coil (CC) bundle domains—canonical CC domains, some of which carry a conserved MADA motif (e.g., ZAR1 and NRCs); RPW8-like domains characteristic of RPW8-like CC-NLRs (CC_R-NLRs) (e.g., NRG1 and ADR1); or G10-type domains (CC_{G10}-NLRs; e.g., RPS2 and RPS5). In many canonical CC-NLRs, activation triggers oligomerization into resistosomes that function as Ca^{2+}-permeable pores, initiating immunity (*9*–*12*).

Canonical CC-NLRs (ZAR1, Sr35) oligomerize into pentameric resistosomes, whereas CC helper NLRs from the NRC clade (NRC2/4) form hexameric resistosomes, both of which target the plasma membrane (*8*, *13*–*18*). By contrast, TIR-NLRs assemble into tetrameric resistosomes that produce chemical signals that indirectly activate downstream CC_R-NLR helpers such as N requirement gene 1 (NRG1) and activated disease resistance 1 (ADR1) (*19*–*21*). Although CC_R-NLRs form oligomers with calcium-channel activity similar to canonical CC-NLR resistosomes, complete structures of CC_R-NLR resistosomes remain unresolved despite recent partial structures of monomeric NRG1 (*6*, *22*–*25*). However, another common feature of the activated CC-NLRs and CC_R-NLRs is localization to distinctive punctate structures in the cell, likely representing clusters of resistosomes, which have been observed through confocal microscopy using C-terminally fused fluorescent tags (*15*, *18*, *26*).

The N-terminal four-helix bundles that execute cell death in plant NLRs are structurally analogous to pore-forming domains in other kingdoms, including mammalian mixed lineage kinase domain–like (MLKL) proteins and fungal heterokaryon incompatibility proteins (*6*, *27*–*29*). Despite this conserved architecture, the amino acid sequences of NLR N-terminal domains that execute immunity are markedly diverse in plants (*17*, *28*). This paradox suggests that resistosome functions may extend beyond the established paradigm of acting as plasma-membrane Ca^{2+} channels. We therefore investigated the CC_R-NLR NRG1, whose divergent N terminus provided an ideal system to investigate whether this architectural variation enables alternative modes of immune activation.

NbNRG1 localizes to multiple subcellular membranes

To understand the activation mechanism of NRG1, we first examined the subcellular localization of NRG1 from the solanaceous model plant *Nicotiana benthamiana* (NbNRG1) in both resting and activated states. Transient expression of full-length NbNRG1:GFP in *N. benthamian* caused cell death (*30*) (fig. S1), hampering live-cell imaging and other cell biology analyses (GFP, green fluorescent protein). To reduce the autoactivity of NbNRG1, we generated a truncated clone of NbNRG1 that lacks the first 14 amino acids of the protein, the most N-terminal region of the CC_R domain ($NbNRG1^{\Delta 14}$). This deletion is equivalent to that previously used for studying *Arabidopsis thaliana* NRG1.1 (AtNRG1.1) (*6*, *25*) (data S1). Transiently expressing $NbNRG1^{\Delta 14}$:GFP triggered weaker cell death than full-length NbNRG1:GFP, making it more suitable for cell biology study (fig. S1). $NbNRG1^{\Delta 14}$ retained the ability to be activated and form punctate structures. Activation occurred upon coexpression with the silencing suppressor p19, which increases transient expression levels, or when activated by the *Xanthomonas* effector XopQ, which is recognized by the TIR-NLR Roq1 in *N. benthamiana* (*31*, *32*). While monitoring the subcellular localization of $NbNRG1^{\Delta 14}$:GFP, we observed atypical punctate fluorescence rather than the uniform peripheral punctate pattern characteristic of plasma-membrane localization, suggesting that activated NbNRG1 may target other membranous compartments. To test for organelle targeting, we coexpressed $NbNRG1^{\Delta 14}$:GFP with red fluorescent protein (RFP)–tagged organelle markers. $NbNRG1^{\Delta 14}$:GFP puncta colocalized with markers for the endoplasmic reticulum (ER) and mitochondria, but not with Golgi or plasma-membrane markers or with a free-RFP control (Fig. 1, A to E). To exclude the possibility that the observed localization was an artifact of the truncated NbNRG1 variant, we optimized full-length NbNRG1 expression to mitigate cell death and imaged cells 26 to 28 hours after agroinfiltration. Full-length NbNRG1:mGOLD, like $NbNRG1^{\Delta 14}$:GFP, localized to organellar compartments rather than the plasma membrane (fig. S2). We next examined whether NbNRG1 activation and localization depends on the canonical XopQ-triggered EDS1-SAG101 signaling cascade. At 24 hours after infiltration, NbNRG1:mTurquoise2 expressed in *N. benthamiana*

[1]Department of Life Sciences, Imperial College London, London, UK. [2]The Sainsbury Laboratory, University of East Anglia, Norwich Research Park, Norwich, UK. [3]Institute of Plant and Microbial Biology, Academia Sinica, Taipei, Taiwan. [4]Cell and Developmental Biology, John Innes Centre, Norwich, UK. ***Corresponding author. Email: o.bozkurt@imperial.ac.uk (T.O.B.); j.kourelis@imperial.ac.uk (J.K.); sophien.kamoun@tsl.ac.uk (S.K.)** †These authors contributed equally to this work.

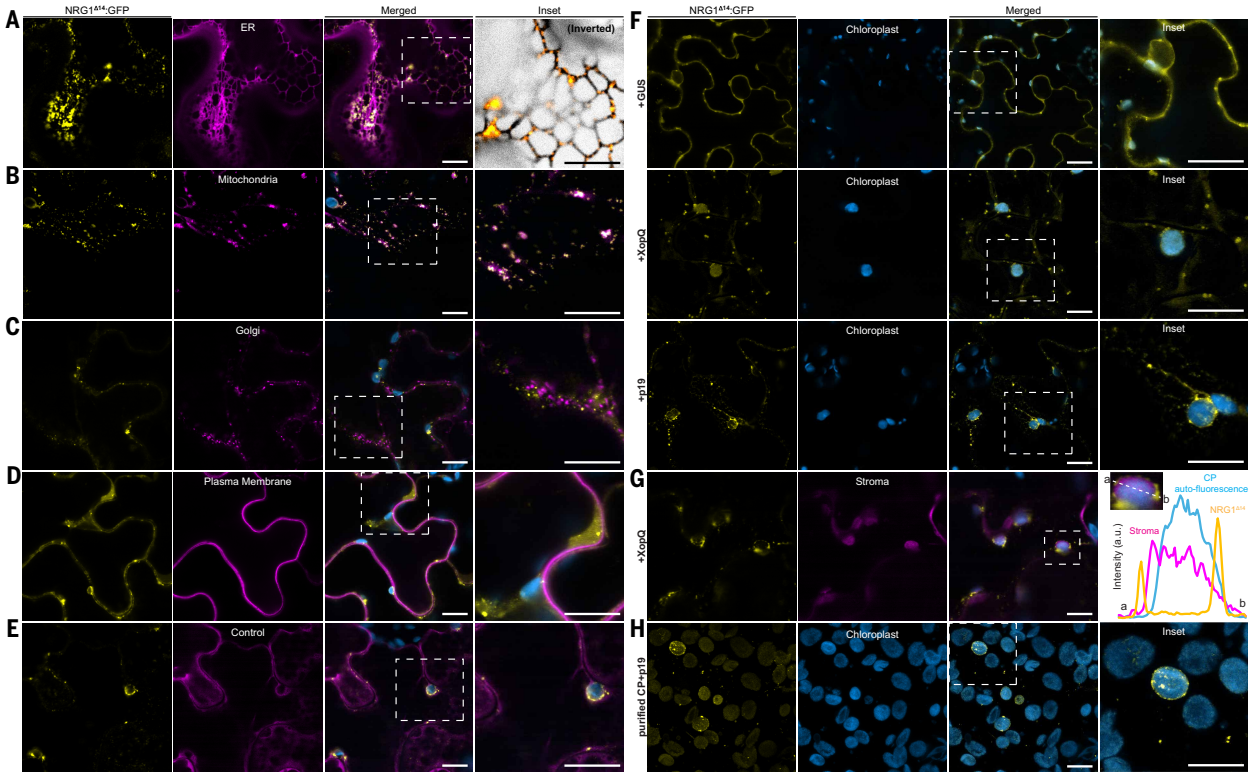

Fig. 1. NbNRG1 targets various subcellular membranous compartments. Confocal micrographs of *N. benthamiana* leaf epidermal cells transiently expressing NbNRG1$^{\Delta 14}$:GFP with (**A**) SP:RFP:HDEL (ER), (**B**) ScCOX41-29:mCherry (mitochondria), (**C**) GmMan11-49:mCherry (Golgi), (**D**) RFP:Remorin1.3 (plasma membrane), and (**E**) RFP:EV (cytoplasm). Dashed boxes in merged panels correspond to the insets. (**F**) Confocal micrographs of *N. benthamiana* leaf epidermal cells transiently expressing NbNRG1$^{\Delta 14}$:GFP with GUS, XopQ, and p19. Dashed boxes in merged panels correspond to the insets. (**G**) Confocal micrographs of *N. benthamiana* leaf epidermal cells transiently expressing NbNRG1$^{\Delta 14}$:GFP with XopQ and CTP1-RFP (stroma). The merged panel highlights chloroplast autofluorescence. Dashed lines in the merged panel correspond to the line intensity plot depicting the relative fluorescence across the marked area. The lines in the intensity plot are colored according to the fluorescent tags used. a.u., arbitrary units. (**H**) Confocal micrographs of purified chloroplasts (CP) from *N. benthamiana* leaf tissue transiently expressing NbNRG1$^{\Delta 14}$:GFP with p19. The dashed box in the merged panel corresponds to the inset. Chloroplasts were visualized using autofluorescence at 648 to 709 nm. All images shown are single-plane images. Scale bars represent 10 μm. Imaging was performed at 2 days after agroinfiltration using a minimum of two leaf patches per sample.

nrg1/adr1 and *eds1/pad4/sag101a/sag101b* (*epss*) knockout (deactivation) plants remained largely cytoplasmic when coexpressed with a β-glucuronidase (GUS) control. Under the same conditions, coexpression with XopQ induced prominent puncta around chloroplasts in *nrg1/adr1* plants but not in *epss* plants. By 2 days after infiltration, XopQ coexpression triggered HR symptoms in *nrg1/adr1* but not *epss* plants. Thus, the canonical EDS1-SAG101 signaling module is required for effector-dependent NRG1 activation and subsequent localization to the chloroplast (fig. S3). To determine whether organelle localization is specific to the CC_R-NLR NbNRG1, we monitored the subcellular localization of an autoactive CC-NLR helper NbNRC4$^{D478V/L9E}$:GFP using the same set of markers (D478V/L9E indicates the mutations Asp^{498}→Val and Leu^{9}→Glu). Consistent with previous reports, NbNRC4$^{D478V/L9E}$ puncta accumulated exclusively at the plasma membrane, with no punctate signal at subcellular membranes or the cytoplasm (*26*) (fig. S4). Thus, the helper CC_R-NLR NbNRG1 undergoes a noncanonical trafficking route upon activation, localizing to multiple endomembranes rather than the plasma membrane, in contrast to the canonical CC-NLR resistosomes (*8*, *18*, *26*).

Activated NbNRG1 localizes to the chloroplast envelope

While examining the various organelle targets of NbNRG1, we noticed that a subset of puncta appeared adjacent to plastids. This prompted us to examine in more detail whether activated NbNRG1 associates with chloroplast membranes. We focused on chloroplasts because they are among the most easily discerned organelles in plant cells. In addition, given the availability of reliable markers, intrinsic autofluorescence that facilitates live-cell imaging, and established tools for functional studies, we focused subsequent analyses on the chloroplast as a tractable model organelle. To monitor NbNRG1 localization in an active state, we coexpressed NbNRG1$^{\Delta 14}$:GFP with XopQ or p19 and observed puncta localization with confocal microscopy. Active NbNRG1$^{\Delta 14}$:GFP displayed a prominent punctate distribution, with a subset of the puncta localizing to chloroplasts (Fig. 1F). By contrast, coexpression with the GUS negative control revealed that resting NbNRG1$^{\Delta 14}$ is cytoplasmic (33% of cells, $n = 12$), consistent with other helper NLRs (*18*, *26*) (Fig. 1F and fig. S5A). Even in the absence of XopQ, NbNRG1$^{\Delta 14}$ retained partial autoactivity with chloroplast-associated puncta observed in 67% of cells ($n = 12$). Upon further activation by XopQ, every examined cell displayed punctate localization (11 of 11 cells), and many puncta were associated with chloroplasts (fig. S5A). Using blue native polyacrylamide gel electrophoresis (PAGE), we confirmed that coexpression with XopQ shifts NbNRG1 into a higher–molecular weight complex, consistent with activation and resistosome formation, linking functional resistosomes to the puncta that were observed (fig. S5D). To pinpoint the chloroplast localization of NbNRG1, we labeled the stroma with CTP1:RFP (*33*). NbNRG1$^{\Delta 14}$:GFP puncta encircled the stromal marker, indicating that NbNRG1 engaged with the chloroplast envelope (Fig. 1G). To confirm chloroplast envelope localization, we used TOC64:GFP as a marker for

the outer chloroplast membrane (*34*). Full-length NbNRG1:mScarlet3 puncta colocalized with TOC64:GFP, demonstrating that NbNRG1 associates with the outer membrane (fig. S6). We also detected NbNRG1:mScarlet3 puncta on stromules, the tubular extensions of chloroplast stroma (*35*). We further validated these live-cell imaging observations with purified chloroplasts, confirming the punctate distribution of NbNRG1$^{\Delta 14}$ on the chloroplast surface (Fig. 1H).

To investigate the subcellular dynamics of resting-state NbNRG1, we tracked its localization pattern under the weaker *Arabidopsis* Act2 promoter (pAct2) and with monomeric fluorescent tags. Unlike p35S::NbNRG1$^{\Delta 14}$:GFP, pAct2::NbNRG1$^{\Delta 14}$:GFP did not cause any visible cell-death symptoms (fig. S5C). Consistent with the lack of cell death, pAct2::NbNRG1$^{\Delta 14}$:GFP showed a weak cytoplasmic signal (78%, $n = 18$ cells), with only few cells displaying detectable puncta, some of which were associated with chloroplasts ($n = 4$ of 18 cells; fig. S5B). To corroborate these results with full-length NbNRG1, we tagged it with the monomeric fluorescent protein mKOk (p35S::NbNRG1:mKOk) (*36*), which also caused weaker cell death than NbNRG1:GFP, enabling live-cell imaging (fig. S5C). NbNRG1:mKOk showed a mixed localization pattern in the few surviving cells. The protein either displayed a cytoplasmic distribution (resting state) or formed punctate structures, some of which localized to chloroplasts in *nrg1* knockout plants ($n = 5$ of 8 images; fig. S7A). This pattern remained similar in *N. benthamiana nrg1/adr1* double knockouts upon coexpression with XopQ or a GUS negative control (fig. S7B). NbNRG1:mKOk remained capable of activation by coexpression with XopQ, forming puncta more frequently (75% of cells, $n = 16$ of 20 images) than the negative control (30% of cells, $n = 6$ of 20 images). Similarly, activation of full-length NbNRG1 expressed from the weaker pAct2 promoter and fused to the bright td8ox2StayGold fluorophore (*37*) produced a prominent punctate pattern, with a subset of puncta surrounding the chloroplasts (fig. S7C). Overall, expression of full-length and truncated NbNRG1 with multiple fluorophores and various promoters, in several genetic backgrounds, showed that resting-state NbNRG1 is largely cytoplasmic but, upon activation, can localize to the chloroplast envelope.

NbNRG1 facilitates calcium efflux from chloroplasts

AtNRG1.1 can oligomerize, form puncta, and channel Ca^{2+}, which are common features of helper NLRs (*6*, *16*). We first established that NbNRG1 elevates cytosolic Ca^{2+}, consistent with prior reports (*6*) (fig. S8). To determine whether NbNRG1 fulfils a similar role at chloroplasts, we coexpressed full-length NbNRG1 fused to mScarlet3 (NbNRG1:mScarlet3) with a stromal Ca^{2+} sensor. We used the genetically encoded calcium sensor GCaMP6s, targeted to the stroma with the RBCS1A transit peptide (RBCS1A-GCaMP6s) (*38*, *39*). Chloroplasts with NbNRG1 puncta displayed markedly lower GCaMP6s fluorescence than neighboring chloroplasts lacking puncta, indicating reduced stromal Ca^{2+} levels (fig. S9). To monitor calcium flux from the chloroplast in the absence of cell death, we deleted the first 20 amino acids of the CC_R domain of NbNRG1 (NbNRG1$^{\Delta 20}$). The NbNRG1$^{\Delta 20}$ truncation completely abolished cell-death symptoms compared with full-length NbNRG1 and NbNRG1$^{\Delta 14}$, yet preserved chloroplast localization (Fig. 2A and fig. S10). To determine whether NbNRG1 requires the N terminus of the CC domain to channel Ca^{2+} from the chloroplast, we coexpressed the stromal Ca^{2+} sensor (RBCS1A-GCaMP6s) with either NbNRG1:mScarlet3, NbNRG1$^{\Delta 20}$:mScarlet3, or GUS:mScarlet3 and quantified the relative sensor fluorescence. Quantitative fluorescence measurements revealed that chloroplasts with full-length NbNRG1:mScarlet3 puncta displayed

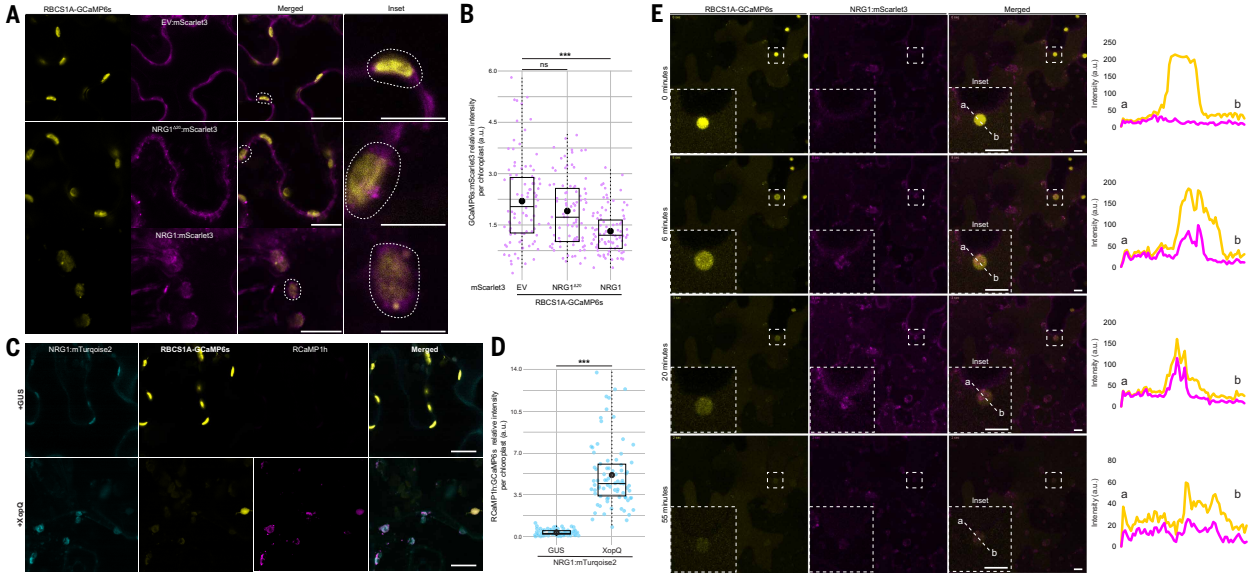

Fig. 2. NbNRG1 facilitates calcium-ion efflux from chloroplasts. (**A**) Confocal micrographs of *N. benthamiana* leaf epidermal cells transiently expressing RBCS1A-GCaMP6s:GFP with EV:mScarlet3, NRG1$^{\Delta 20}$:mScarlet3, or NRG1:mScarlet3. Dashed boxes in merged panels correspond to the insets, which show representative chloroplasts used to measure the relative GCaMP6s:mScarlet3 intensity in (B). (**B**) Box and dot plot showing GCaMP6s:mScarlet3 relative intensity per chloroplast for 90 chloroplasts. Each chloroplast is shown as a lilac dot; black dots indicate the mean. Asterisks indicate statistical comparison of NRG1Δ20:mScarlet3 or NRG1:mScarlet3 with EV:mScarlet3 control [NRG1$^{\Delta 20}$:mScarlet3 – Wilcoxon signed-rank test, $W = 3446$, $P = 0.208$ (ns, not significant); NRG1:mScarlet3 – Wilcoxon, $W = 5511$, $^{***}P < 0.005$]. EV, empty vector. (**C**) Confocal micrographs of *nrg1/adr1* knockout *N. benthamiana* leaf epidermal cells expressing RBCS1A-GCaMP6s:GFP, RCaMP1h, and NRG1:mTurquoise2 with or without XopQ. Imaging was performed 26 to 28 hours after agroinfiltration using at least two leaf patches per sample. Raw fluorescence data are provided in data S2. (**D**) Box and dot plot showing RCaMP1h:GCaMP6s relative intensity per chloroplast for 80 chloroplasts. Each chloroplast is shown as a turquoise dot; black dots indicate the mean. Asterisks indicate statistical comparison of XopQ coexpression with the GUS control (Wilcoxon signed-rank test, $W = 2$, $^{***}P < 0.005$). (**E**) Confocal micrographs of *N. benthamiana* leaf epidermal cells expressing NRG1:mScarlet3 and RBCS1A-GCaMP6s:GFP from a 1-hour–time series movie collected 27 to 28 hours after agroinfiltration. Insets correspond to dashed boxes in the overview panels, with line intensity plots across the marked region (a–b). A second movie from an independent experiment is shown in fig. S11. All images shown are single-plane images. Scale bars represent 10 μm.

the greatest reduction in stromal GCaMP6s signal, which was significantly lower than that seen with either NbNRG1$^{\Delta 20}$ or the GUS:mScarlet3 control (Fig. 2, A and B). To examine Ca^{2+} flux upon XopQ activation, we coexpressed full-length NRG1:mTurquoise2 with chloroplast (RBCS1A-GCaMP6s) and cytoplasmic (RCaMP1h) Ca^{2+} sensors (*40*). Relative to the GUS control, activation by XopQ induced NRG1:mTurquoise2 puncta on the chloroplast envelope and a marked increase in the RCaMP1h:GCaMP6s fluorescence ratio, consistent with Ca^{2+} efflux from the chloroplast into the cytoplasm (Fig. 2, C and D).

To elucidate the temporal dynamics of NbNRG1-dependent depletion of Ca^{2+} from the chloroplast, we tracked stromal Ca^{2+} sensor (RBCS1A-GCaMP6s) fluorescence over time on various chloroplasts in cells labeled by NbNRG1:mScarlet3. Time-lapse imaging over 60 min linked NbNRG1 activation directly to Ca^{2+} export. As NbNRG1:mScarlet3 shifted from a diffuse cytoplasmic localization to a punctate signal surrounding chloroplasts, stromal GCaMP6s fluorescence declined in the same chloroplasts (Fig. 2E and fig. S11). Subsequently, an overall reduction in NbNRG1:mScarlet3 was observed with the onset of cell death. This finding indicated that puncta formation at the chloroplast envelope directly corresponds to Ca^{2+} efflux from the stroma. Thus, upon activation, NbNRG1 acts at the chloroplast envelope to mediate Ca^{2+} release from the chloroplast stroma into the cytosol, and this channeling activity depends on the integrity of the most N-terminal region of the CC domain.

CC_R-NLRs possess an extended N terminus relative to canonical CC-NLRs

The distinct membrane-targeting and Ca^{2+}-channeling activities of NbNRG1 at organellar membranes imply evolutionary divergence from the plasma membrane–centric mechanism of canonical CC-NLRs. To clarify the sequence diversity of the N terminus of CC_R-NLRs, we searched for N-terminal motifs in CC_R-NLRs across land plants, using canonical CC-NLRs as an outgroup (fig. S12 and data S4 to S12). As previously reported, canonical CC-NLRs, including ZAR1, Sr35, and the NRC clade members, share a conserved N-terminal MADA motif that is required for cell-death function and is orientated toward the plasma membrane upon resistosome formation (*6*, *7*, *16*, *41*). By contrast, CC_R-NLRs showed several distinct N-terminal motifs across the land plants, with an initial divergence of two CC_R-NLR groups in the monilophytes and the gymnosperms. Subsequently, ADR1- and NRG1-specific N-terminal motifs appear to have evolved during divergence of the angiosperms. Thus, unlike canonical CC-NLRs, CC_R-NLRs evolved multiple distinctive N-terminal motifs during the evolution of land plants.

Given that NbNRG1 targets organelle membranes, we asked whether this feature is encoded in its distinctive N-terminal architecture and whether this enables the NbNRG1 resistosome to function at membranes beyond the plasma membrane. To address this, we examined the structural divergence of the N-terminal helices of CC_R-NLRs. Because no resolved structures of activated CC_R-NLR resistosomes are available, we modeled CC_R-NLR oligomers using AlphaFold 3 (AF3) and compared them with experimental structures of CC-NLR resistosomes (*14*, *42*). AF3 predictions revealed that CC_R-NLR resistosomes possess a markedly elongated CC funnel relative to that of canonical CC-NLRs (Fig. 3A, fig. S13, and data S13). The NbNRG1 funnel extends ~50 Å beyond those of ZAR1, Sr35, and NRC4, potentially exceeding the thickness of a single lipid bilayer (*43*) (Fig. 3A). Predictions of the resting state likewise revealed a distinctively extended fourth α helix in NbNRG1 that is absent from canonical CC-NLRs (fig. S14). We also used AF3 to evaluate the truncated variants that we used in our studies (NbNRG1$^{\Delta 14}$ and NbNRG1$^{\Delta 20}$). Both formed intact CC domain structures similar to those of full-length NbNRG1 but with shorter N-terminal regions (fig. S15A), reinforcing the functional importance of the extended CC domain (Fig. 2, A and B, and figs. S5 and S10). Analysis of the electrostatic potential of the predicted NbNRG1 CC domain revealed, as observed for *A. thaliana* NRG1 (*25*), positive, negative, and neutral regions at the periphery, lumen, and outer surface, respectively (fig. S15, B and C). Overall, these in silico analyses indicate that NbNRG1 possesses an extended CC domain architecture relative to canonical CC-NLRs, which may underlie its ability to target diverse membrane compartments.

Enrichment of canonical CC-NLR NbNRC4 at the chloroplast abolishes its activity

Ca^{2+} channeling and downstream HR functions are conserved among canonical CC-NLRs and CC_R-NLRs, yet their CC domains are predicted to differ sharply in length (Fig. 3A and fig. S14). Because the elongated CC_R domain of NbNRG1 is essential for Ca^{2+} efflux from chloroplasts (Fig. 2, A and B, and figs. S9, S11, and S15), we asked whether the shorter CC domain of the CC-NLR helper NbNRC4 could perform the same function. To address this, we redirected the autoactive NbNRC4^{D478V}:GFP and full-length NbNRG1:GFP to the chloroplast surface by coexpression with a GFP-binding nanobody anchored in the chloroplast outer envelope by fusion with the N terminus of CHUP1 (CP:LaG-24) (*44*, *45*) (Fig. 3, B to D). Nanobody trapping at the chloroplast did not significantly alter the soluble levels of either NbNRG1:GFP, NbNRC4^{D478V}:GFP, or GFP control, although protein levels for NbNRC4^{D478V} with or without CP:LaG-24 were lower than those for NbNRG1 (fig. S16). Chloroplast trapping abolished the HR function of NbNRC4^{D478V}:GFP but not that of NbNRG1:GFP (Fig. 3, B to D). Our stromal Ca^{2+} measurements with the red-fluorescent sensor RBCS1A-jRGECO1a mirrored these phenotypes (*39*, *46*). NbNRG1 trapped at the chloroplast envelope depleted stromal Ca^{2+} stores, but NbNRC4^{D478V} and the GFP control did not, showing significantly higher sensor:GFP ratios than NbNRG1 (fig. S17). As a control, we trapped NbNRG1:GFP and NbNRC4^{D478V}:GFP at the plasma membrane using the same anti-GFP nanobody (Lti6b:LaG-24 or PIP2a:LaG-24) (*45*, *47*). Trapping did not affect HR activity (fig. S18), confirming that cell-death function was intact. For NbNRG1, although a fraction of protein escaped to its native location, residual puncta showed that some was still retained at the plasma membrane. Thus, the distinct CC_R domain architecture of divergent helper NLRs allows them to function at specific membrane interfaces.

The extended fourth α helix underpins NbNRG1 membrane targeting and HR activities

Compared with canonical CC-NLRs, NbNRG1 contains a distinctively extended fourth α helix (fig. S14), which has been previously shown to be essential for HR function in *Arabidopsis* NRG1 variants (*6*, *25*). To determine how this region contributes to organellar targeting, we generated single- and double-point mutants within this extended helix (Fig. 3, E and F, and fig. S19). Single mutants, NbNRG1^{K126E}:GFP (Lys^{126}→Glu) and NbNRG1^{L129E}:GFP (Leu^{129}→Glu), exhibited partial organelle and plasma membrane localization and retained HR activity similar to that of wild-type NbNRG1 (Fig. 3, E and F, and fig. S19), consistent with the incomplete plasma membrane trapping observed previously with Lti6b:LaG-24 and PIP2a:LaG-24 nanobodies (fig. S18). By contrast, the double mutant NbNRG1$^{K126E/L129E}$:GFP was fully retained at the plasma membrane and showed a marked reduction in HR (Fig. 3, E and F, and fig. S19), indicating that exclusive plasma membrane localization impairs NbNRG1's cell-death execution function. Both K126 and L129 face the outside of the NbNRG1 CC funnel and do not alter the predicted pore architecture (Fig. 3E), consistent with NbNRG1$^{K126E/L129E}$:GFP retaining HR activity relative to the pore-deficient NbNRG1$^{\Delta 20}$:GFP control (fig. S19, A and B). These residues are also distal to the EDS1-SAG101 interaction surface on NRG1 (*22*, *23*), suggesting that upstream activation is likely preserved and that the observed phenotype primarily reflects altered membrane targeting. Protein levels mirrored these phenotypes. NbNRG1$^{K126E/L129E}$:GFP accumulated to higher levels than the single mutants and wild-type NbNRG1, consistent with reduced cell death (fig. S19C). Thus, the extended fourth α helix is the critical structural element that directs

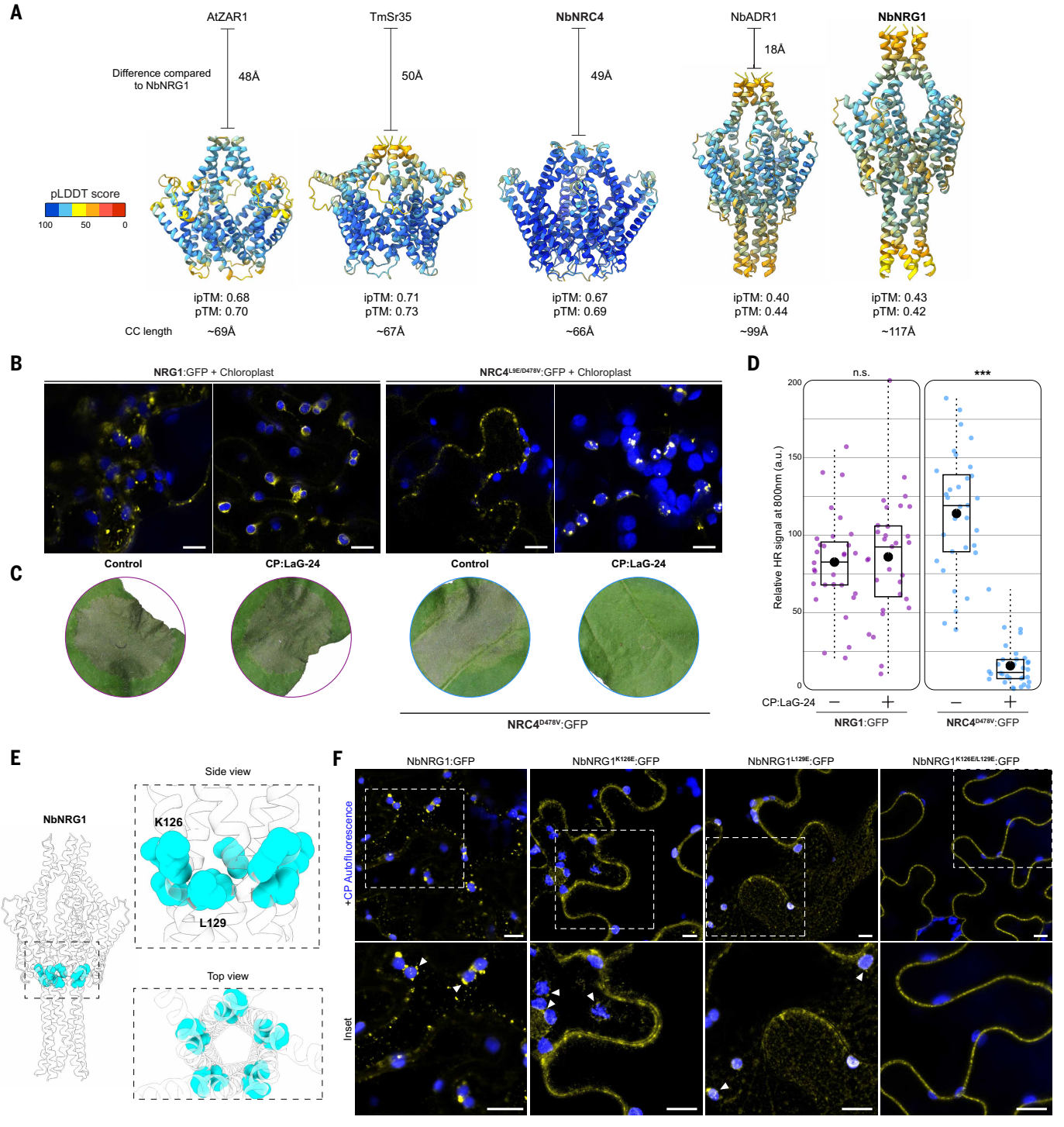

Fig. 3. An extended CC domain architecture enables NbNRG1 organellar targeting. (**A**) AF3-predicted CC domain models of AtZAR1, TmSr35, NbNRC4, NbADR1, and NbNRG1 colored by predicted local distance difference test (pLDDT) values. NbNRG1 and NbADR1 were modeled as pentamers based on higher predicted template modeling (pTM) and interface pTM (ipTM) scores relative to hexameric models. Differences in angstroms relative to the NbNRG1 CC domain are indicated, with total CC domain lengths shown below each structure. An AF3 confidence analysis is shown in fig. S13. (**B**) Confocal micrographs of *N. benthamiana* leaf epidermal cells transiently expressing NbNRG1:GFP or NRC4$^{L9E/D478V}$:GFP with control or NtHR:LaG-24 (CP:LaG-24). Chloroplasts were visualized by autofluorescence (648 to 709 nm). The images shown are single-plane images. Scale bars represent 10 μm. Imaging was performed using at least two leaf patches from different plants. (**C**) Representative leaf images from *N. benthamiana* showing HR after expression of NRG1:GFP or NRC4^{D478V}:GFP with CP:LaG-24 nanobody or control. (**D**) Box and dot plot showing normalized HR signal at 800 nm (infrared) for 31 leaves from two technical replicates. Leaves are colored purple (NRG1:GFP) or blue (NRC4^{D478V}:GFP); black dots indicate means. Asterisks indicate the statistical comparison of CP:LaG-24 treatment versus control [NRG1:GFP – Student's *t* test, $P = 0.7089$ (n.s., not significant); NRC4D478V:GFP – Wilcoxon signed-rank test, $W = 7$, $^{***}P < 0.005$]. Raw HR data are provided in data S3. (**E**) AF3 model of NbNRG1 highlighting residues K126 and L129 (light blue). (**F**) Confocal micrographs of *nrg1/adr1* knockout *N. benthamiana* leaf epidermal cells expressing NRG1:GFP, NRG1^{K126E}:GFP, NRG1^{L129E}:GFP, or NRG1$^{K126E/L129E}$:GFP. Chloroplasts were visualized by autofluorescence (648 to 709 nm). Images shown are single-plane images; dashed boxes correspond to the insets. Scale bars represent 10 μm. Imaging was performed using at least two leaf patches per condition.

NbNRG1 to the correct organellar membrane environment and is essential for its HR execution function.

Chloroplast targeting is a conserved feature among plant CC_R-NLRs

Given the evolution of specific N-terminal motifs in CC_R-NLRs across the land plants, we wondered whether chloroplast targeting is a conserved feature of CC_R-NLRs. To investigate the conservation of chloroplast targeting, we examined the subcellular localization of five CC_R-NLRs that span ~360 million years of land-plant divergence (Fig. 4A). We selected four NRG1 subclass members from across the angiosperms, as well as one from the monilophytes predating the divergence of the NRG1 and ADR1 subclasses, which are the only CC_R-NLR subclasses found in flowering plants (fig. S12). All five CC_R-NLRs accumulated as discrete puncta on the chloroplast outer membrane (Fig. 4B) and, like NbNRG1, had extended CC domain structures compared with the canonical CC-NLR NbNRC4 (fig. S20). These observations extend our findings beyond the model species *N. benthamiana* and suggest that chloroplast targeting is a conserved feature of NRG1-like CC_R-NLRs, possibly predating the divergence of monilophytes and seed plants more than 360 million years ago (*48*).

Discussion

CC_R-NLRs constitute one of the oldest NLR clades, persisting from mosses to angiosperms (*9*). Despite the conserved four-helix CC bundle, CC-NLR N termini are highly diverse, suggesting that they encode functional specialization. For NbNRG1, the distinctively extended fourth α helix appears to act as a membrane-targeting module that helps fine-tune where immune signaling is executed.

In this context, it is notable that *Arabidopsis* NRG1 variants also carry an extended fourth helix, yet previous studies have so far reported primarily plasma membrane–localized resistosomes (*6*, *25*). These analyses were largely performed with autoactive AtNRG1 alleles expressed in *N. benthamiana* rather than with native *Arabidopsis* NRG1 activated in its endogenous cellular environment. Experiments were not necessarily designed to systematically probe potential organelle localization. Our mutational data show that modest changes in the fourth α helix are sufficient to switch NbNRG1 between chloroplast and

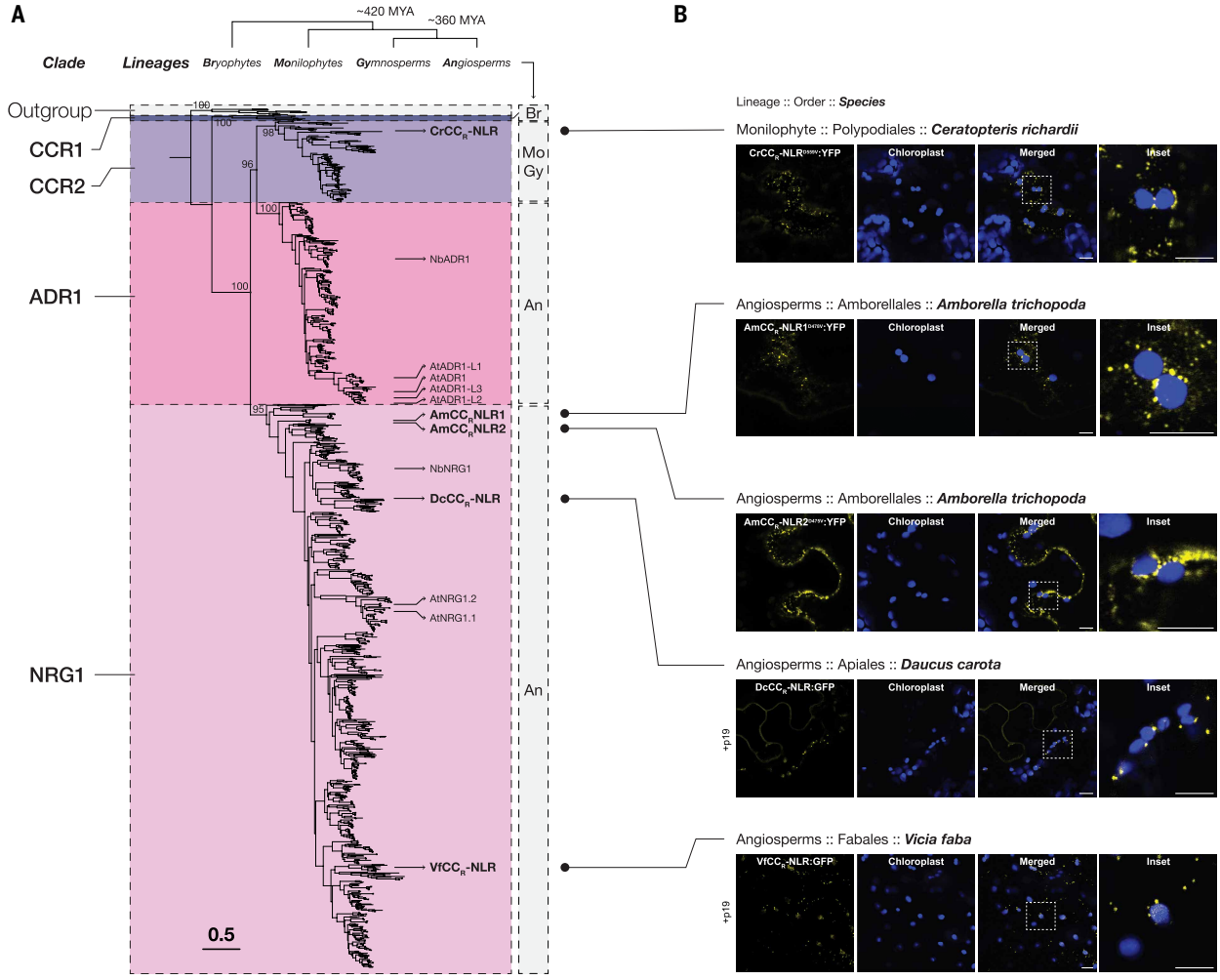

Fig. 4. Chloroplast targeting is a conserved feature among CC_R-NLRs. (**A**) The phylogenetic tree illustrates the relationships among 56,280 CCR-NLRs based on their NB-ARC domain sequences. Four well-supported clades are highlighted: the CCR1 and CCR2 clades (purple), the ADR1 clade (pink), and the NRG1 clade (lilac). The tree is rooted with sequences from AtZAR1, NbZAR1, and NRCs from tomato as the outgroup. MYA, million years ago. (**B**) Confocal micrographs of *N. benthamiana* leaf epidermal cells transiently expressing C-terminally yellow fluorescent protein (YFP)– or GFP-fused NRG1-like CC_R-NLRs identified from the phylogenetic analysis in (A). Silencing suppressor p19 was coexpressed with wild-type *Daucus carota* CC_R-NLR ($DcCC_R$-NLR) and *Vicia faba* CC_R-NLR ($VfCC_R$-NLR). For *Ceratopteris richardii* CC_R-NLR ($CrCC_R$-NLR) and *Amborella trichopoda* CC_R-NLR1/2 ($AmCC_R$-NLR1/2), autoactive D to V mutants were coupled with L-to-E mutations in the first α helix to allow imaging. Chloroplasts were visualized using autofluorescence at 648 to 709 nm. All images shown are single-plane images. Dashed boxes in merged panels correspond to the insets. Scale bars represent 10 μm.

plasma membrane targeting. A full exploration of whether *Arabidopsis* NRG1 can also access organellar membranes will require further analysis.

The ability of NRG1 to target calcium-rich organelles such as chloroplasts, mitochondria, and the ER may enable it to tap into alternative intracellular calcium stores, diversifying the cell-death immune response (*49*) (fig. S21). Using multiple Ca^{2+} sensors for the chloroplast stroma and the cytoplasm, we demonstrate that, upon activation by the bacterial effector XopQ, the distinctive localization pattern of NbNRG1 at the chloroplast envelope is indeed followed by Ca^{2+} efflux and that the extended length of the NbNRG1 CC domain is necessary for cation channeling from the chloroplast. By diversifying its subcellular localization, NRG1 may have evolved to initiate immune responses through multiple membrane interfaces. This could represent a multicompartmental defense strategy to counteract pathogen effectors that suppress activated NLR functions at the plasma membrane and therefore sustain robust immunity. Notably, the chloroplast outer envelope is ~50 to 60 Å thick (*43*), comparable to the ~50-Å CC-funnel length difference between NbNRG1 and NbNRC4 (Fig. 3A), which is consistent with NbNRG1 being structurally suited to engage double-membrane organelles.

The localization of NbNRG1 to organelles supports a model in which NLR-mediated immune signaling is more compartmentalized and complex than anticipated. Our findings align with recent research that emphasizes the critical role of chloroplasts in immunity (*50*, *51*). Upon immune activation, chloroplasts down-regulate photosynthesis and produce reactive oxygen species (ROS) and defense hormones and facilitate signaling through the mitogen-activated protein kinase (MAPK) pathway (*49*–*56*), processes that are tightly linked to NLR-mediated immunity. We observed NRG1 puncta at the stromules, which act as conduits to transport prodefense signals, such as ROS (*35*). In addition to mediating Ca^{2+} efflux, activated NRG1 may interact with these chloroplast immune processes, further linking organellar function to NLR-triggered immunity.

Our findings reveal hidden functional diversity among CC domain NLRs, with sequence features such as N-terminal extensions fine-tuning membrane preference and channel activity. Decoding this permissive-membrane tethering code could enable the engineering of membrane-tuned NLRs for more versatile and durable plant immunity.

REFERENCES AND NOTES

1. Z. Duxbury, C. H. Wu, P. Ding, *Annu. Rev. Plant Biol.* **72**, 155–184 (2021).
2. B. Sundaram, R. E. Tweedell, S. Prasanth Kumar, T. D. Kanneganti, *Immunity* **57**, 674–699 (2024).
3. C. L. Evavold *et al.*, *Cell* **184**, 4495–4511.e19 (2021).
4. N. Kayagaki *et al.*, *Nature* **526**, 666–671 (2015).
5. E. Pitsili, U. J. Phukan, N. S. Coll, *Cold Spring Harb. Perspect. Biol.* **12**, a036483 (2020).
6. P. Jacob *et al.*, *Science* **373**, 420–425 (2021).
7. J. Wang *et al.*, *Science* **364**, eaav5870 (2019).
8. G. Bi *et al.*, *Cell* **184**, 3528–3541.e12 (2021).
9. K. S. Chia, P. Carella, *New Phytol.* **240**, 496–501 (2023).
10. M. P. Contreras, D. Lüdke, H. Pai, A. Toghani, S. Kamoun, *EMBO Rep.* **24**, e57495 (2023).
11. S. Shepherd, E. L. H. Yuen, P. Carella, T. O. Bozkurt, *Curr. Opin. Plant Biol.* **74**, 102372 (2023).
12. E. L. H. Yuen, S. Shepherd, T. O. Bozkurt, *Annu. Rev. Phytopathol.* **61**, 325–350 (2023).
13. A. Förderer *et al.*, *Nature* **610**, 532–539 (2022).
14. M. P. Contreras *et al.*, *Sci. Adv.* **9**, eadg3861 (2023).
15. M. P. Contreras *et al.*, *EMBO J.* **42**, e111519 (2023).
16. F. Liu *et al.*, *Cell* **187**, 4877–4889.e15 (2024).
17. J. Madhuprakash *et al.*, *Sci. Adv.* **10**, eadr2594 (2024).
18. M. Selvaraj *et al.*, *PLOS Biol.* **22**, e3002868 (2024).
19. S. Ma *et al.*, *Science* **370**, eabe3069 (2020).
20. R. Martin *et al.*, *Science* **370**, eabd9993 (2020).
21. B. Castel *et al.*, *New Phytol.* **222**, 966–980 (2019).
22. S. Huang *et al.*, *Nature* **639**, 447–455 (2025).
23. Y. Xiao *et al.*, *Nature* **639**, 438–446 (2025).
24. J. M. Feehan *et al.*, *Proc. Natl. Acad. Sci. U.S.A.* **120**, e2210406120 (2023).
25. Z. Wang *et al.*, *Proc. Natl. Acad. Sci. U.S.A.* **120**, e2222036120 (2023).
26. C. Duggan *et al.*, *Proc. Natl. Acad. Sci. U.S.A.* **118**, e2104997118 (2021).
27. A. R. Bentham, R. Zdrzalek, J. C. De la Concepcion, M. J. Banfield, *Plant Cell Physiol.* **59**, 2398–2408 (2018).
28. K. S. Chia *et al.*, *Plant Cell* **36**, 2491–2511 (2024).
29. A. Daskalov *et al.*, *Proc. Natl. Acad. Sci. U.S.A.* **113**, 2720–2725 (2016).
30. J. R. Peart, P. Mestre, R. Lu, I. Malcuit, D. C. Baulcombe, *Curr. Biol.* **15**, 968–973 (2005).
31. R. A. L. Van Der Hoorn, S. Rivas, B. B. H. Wulff, J. D. G. Jones, M. H. A. J. Joosten, *Plant J.* **35**, 305–315 (2003).
32. T. Qi *et al.*, *Proc. Natl. Acad. Sci. U.S.A.* **115**, E10979–E10987 (2018).
33. B. Petre *et al.*, *Cell. Microbiol.* **18**, 453–465 (2016).
34. F. K. H. Breuers *et al.*, *Front. Plant Sci.* **3**, 7 (2012).
35. J. L. Caplan *et al.*, *Dev. Cell* **34**, 45–57 (2015).
36. H. Tsutsui, S. Karasawa, Y. Okamura, A. Miyawaki, *Nat. Methods* **5**, 683–685 (2008).
37. R. Ando *et al.*, *Nat. Methods* **21**, 648–656 (2024).
38. T. W. Chen *et al.*, *Nature* **499**, 295–300 (2013).
39. A. O. Nedo *et al.*, *New Phytol.* **244**, 1864–1881 (2024).
40. Y.-F. Chen *et al.*, *Proc. Natl. Acad. Sci. U.S.A.* **123**, e2523470123 (2026).
41. H. Adachi *et al.*, *eLife* **8**, e49956 (2019).
42. A. Toghani *et al.*, *New Phytol.* **248**, 17–23 (2025).
43. D. Glushkova, S. Böhm, M. Beck, *J. Cell Biol.* **225**, e202504053 (2026).
44. K. Oikawa *et al.*, *Plant Physiol.* **148**, 829–842 (2008).
45. P. C. Fridy *et al.*, *Nat. Methods* **11**, 1253–1260 (2014).
46. H. Dana *et al.*, *eLife* **5**, e12727 (2016).
47. A. Martinière *et al.*, *Proc. Natl. Acad. Sci. U.S.A.* **109**, 12805–12810 (2012).
48. J. L. Morris *et al.*, *Proc. Natl. Acad. Sci. U.S.A.* **115**, E2274–E2283 (2018).
49. S. Stael *et al.*, *J. Exp. Bot.* **63**, 1525–1542 (2012).
50. P. Kachroo, T. M. Burch-Smith, M. Grant, *Annu. Rev. Phytopathol.* **59**, 423–445 (2021).
51. E. L. H. Yuen *et al.*, *Plant Cell* **37**, koaf214 (2025).
52. M. de Torres Zabala *et al.*, *Nat. Plants* **1**, 15074 (2015).
53. C. Gao *et al.*, *Proc. Natl. Acad. Sci. U.S.A.* **117**, 9613–9620 (2020).
54. J. Jelenska *et al.*, *Curr. Biol.* **17**, 499–508 (2007).
55. Q. Xu *et al.*, *Nat. Commun.* **10**, 5571 (2019).
56. J. Su *et al.*, *PLOS Biol.* **16**, e2004122 (2018).
57. F. King *et al.*, A helper NLR channels organellar calcium to trigger plant immunity, Version 3. Zenodo (2026); https://doi.org/10.5281/zenodo.18593781.
58. A. Toghani, amiralito/NRG1_Localization: Repository release, Version 1. Zenodo (2026); https://doi.org/10.5281/zenodo.18866308.

ACKNOWLEDGMENTS

We thank the Imperial College FILM facility for their technical expertise and provision of our microscopy equipment. **Funding:** This work was funded by Biotechnology and Biological Sciences Research Council (BBSRC) Impact Acceleration Fund BB/X511055/1 (T.I.); Bezos Earth Fund through the Bezos Centre for Sustainable Protein BCSP/IC/001 (T.O.B.); BBSRC BB/X016382/1 (E.L.H.Y. and T.O.B.); National Science and Technology Council NSTC-112-2628-B-001-007 and NSTC 113-2927-I-001-514 (H.-Y.W. and C.-H.W.); The Gatsby Charitable foundation (A.T., S.K., B.C., and J.D.G.J.); BBSRC BB/P012574 (Plant Health ISP) (A.T. and S.K.); BBSRC BBS/E/J/000PR9795 (A.T. and S.K.); BBSRC BBS/E/J/000PR9796 (Plant Health ISP – Response) (A.T. and S.K.); BBSRC BBS/E/J/000PR9797 (Plant Health ISP – Susceptibility) (A.T. and S.K.); BBSRC BBS/E/J/000PR9798 (Plant Health ISP – Evolution) (A.T. and S.K.); BBSRC BB/V002937/1 (A.T. and S.K.); BBSRC BB/Y514201/1 (J.K.); UK Research and Innovation (UKRI) EP/Y032187/1 (A.T. and S.K.); European Research Council (ERC) BLASTOFF 743165 (A.T. and S.K.); and BBSRC BB/X010996/1 (Advancing Plant Health) (K.-S.C. and P.C.). **Author contributions:** Conceptualization: T.I., F.J.K., J.K., T.O.B.; Methodology: T.I., F.J.K., A.T., J.K., T.O.B.; Investigation: T.I., F.J.K, L.W., S.J., E.L.H.Y., H.-Y.W., A.T., J.K., C.V., N.E., V.A., K.-S.C., B.C., T.O.B.; Visualization: T.I., E.L.H.Y., A.T., T.O.B.; Funding acquisition: T.O.B., C.-H.W., S.K., J.D.G.J., P.C.; Project administration: T.I., F.J.K., J.K., T.O.B.; Supervision: T.I., T.O.B., C.-H.W., S.K., J.D.G.J., P.C.; Writing – original draft: T.I., F.J.K., T.O.B; Writing – review & editing: T.I., F.J.K., E.L.H.Y., A.T., J.K., S.K., J.D.G.J., C.-H.W., P.C., T.O.B. **Competing interests:** T.O.B. and S.K. receive funding from industry and cofounded a start-up company (Resurrect Bio Ltd.) on NLR biology. S.K. and J.K. are inventors on patent EP4419694A1 held by The Sainsbury Laboratory on receptor-nanobody fusions. P.C. and K.-S.C. are inventors on patent application PC933754WO submitted by the John Innes Centre that covers nonflowering plant NLRs. S.K. is an inventor on patent application WO2025191167A1 submitted by Limagrain Europe and the patent MX2025006485A held by Resurrect Bio on NLR biology. **Data, code, and materials availability:** Constructs generated for this study will be made available upon request. All data are available in the main text or the supplementary materials. Data S1 to S13 and all other supplementary materials have been deposited on Zenodo (*57*), and all scripts used in this study have been deposited on Zenodo (*58*). This research was funded in whole or in part by UKRI (BB/P012574, BBS/E/J/000PR9795, BBS/E/J/000PR9796, BBS/E/J/000PR9797, BBS/E/J/000PR9798, BBSRC BB/V002937/1, BBSRC BB/Y514201/1, BBSRC BB/X010996/1, and EP/Y032187/1), a cOAlition S organization, and by the ERC (BLASTOFF 743165); as required, the author will make the Author Accepted Manuscript (AAM) version available under a CC BY public copyright license.

SUPPLEMENTARY MATERIALS

science.org/doi/10.1126/science.aeb6690
Materials and Methods; Figs. S1 to S21; Tables S1 and S2; References (*59*–*82*); MDAR Reproducibility Checklist; Data S1 to S13

Submitted 21 August 2025; resubmitted 28 November 2025; accepted 12 March 2026
10.1126/science.aeb6690

A helper NLR channels organellar calcium to trigger plant immunity

Tarhan Ibrahim, Freddie J. King, AmirAli Toghani, Luyao Wang, Saskia Jenkins, Enoch Lok Him Yuen, Hung-Yu Wang, Cristina Vuolo, Nick Eilmann, Vanda Adamkova, Khong-Sam Chia, Baptiste Castel, Jonathan D. G. Jones, Philip Carella, Chih-Hang Wu, Jiorgos Kourelis, Sophien Kamoun, and Tolga O. Bozkurt

Science **392** (6797), . DOI: 10.1126/science.aeb6690

Editor's summary

Plant nucleotide-binding leucine-rich repeat (NLR) immune receptors form resistosome complexes thought to function primarily at the plasma membrane. Ibrahim *et al*. found that the helper NLR NRG1 instead targets the chloroplast envelope, channeling stromal calcium into the cytosol. AlphaFold modeling indicated that NRG1's N-terminal coiled-coil domain is longer than that of canonical coiled coil-type NLRs, enough to span the double chloroplast membrane. All tested orthologs of NRG1 across approximately 360 million years of plant evolution also targeted chloroplasts, suggesting that this compartment-specific immune mechanism is ancient. —Unnati Sonawala and Madeleine Seale